

ARTICLE OPEN



CMTJ: Simulation package for analysis of multilayer spintronic devices

Jakub Mojsiejuk¹✉, Sławomir Ziętek¹✉, Krzysztof Grochot^{1,2}, Witold Skowroński¹ and Tomasz Stobiecki^{1,2}

We present *CMTJ*—a simulation package for large-scale macrospin analysis of multilayer spintronics devices. Apart from conventional simulations, such as magnetoresistance and magnetisation hysteresis loops, *CMTJ* implements a mathematical model of dynamic experimental techniques commonly used for spintronics devices characterisation, for instance: spin diode ferromagnetic resonance, pulse-induced microwave magnetometry, or harmonic Hall voltage measurements. We find that macrospin simulations offer a satisfactory level of agreement, demonstrated by a variety of examples. As a unified simulation package, *CMTJ* aims to accelerate wide-range parameter search in the process of optimising spintronics devices.

npj Computational Materials (2023)9:54; <https://doi.org/10.1038/s41524-023-01002-x>

INTRODUCTION

Modern development of spintronic devices¹ requires careful design and a time-consuming fabrication process, a preparation of which is often carried out with the help of simulations. The use of magnetic materials and multilayer structures with certain material parameters enables the creation of a spintronic device with optimal functionality, depending on the application: good memory is characterised by high endurance and energy-efficient write operations², sensor development usually focuses on high sensitivity and low inherent noise³, and in devices with a high-frequency component, we aim to maximise the quality factor while retaining low energy consumption⁴. To simulate such a variety of use cases, we need an extensive simulation toolkit. As we climb from the macromagnetic models, steadily increasing the resolution of the phenomena in atomistic simulations, and finally reaching the *ab initio* simulations, we do so with increasing computational cost. This computational cost is closely correlated with the number and complexity of the simulation parameters and may hamper the speed of prototyping. Consequently, we are facing the dilemma of choosing between a slower, but accurate approach and a faster, but not as precise method.

Micromagnetic packages, such as *MUMAX3*⁵ and *OOMMF*⁶, offer a lot of plasticity in modelling magnetic interactions of complex structures while maintaining an acceptable computational cost. On the other side of the spectrum, *VASP*⁷ and *QUANTUM ESPRESSO*^{8,9} lead the way as recognised self-consistent solvers. Between them, there are tools for atomistic magnetic simulations such as *VAMPIRE*¹⁰ or *SPIRIT*¹¹ that, in addition to dynamics solvers, can also employ Monte Carlo methods for time-independent processes. In the micromagnetic regime, a notable research direction was devoted to creating magnetic tunnel junction (MTJ) behavioural models in Verilog, for example, in the work of R. Garg et al.¹² or T. Chen et al.^{13,14}. Such models attempt to capture the electronic nature of spintronics devices, describing them as discrete elements or electronic elements in a circuit, making it easy to prototype devices composed of discrete components.

In this article, we seek to fill a gap in the magnetic simulation hierarchy by providing an open-source, computationally efficient standardised Python package, *CMTJ*, for rapid prototyping, large-

scale parameter search, and macrospin simulation of multilayer systems. *CMTJ* is capable of simulating, for example, current-induced magnetisation dynamics calculations originating from spin transfer torque (STT)^{15,16} such as spin torque oscillator (STO)¹⁷, STT-induced magnetisation switching¹⁸ or voltage-controlled magnetic anisotropy (VCMA) phenomena¹⁹. Some of those motivating examples are shown in Fig. 1. In the text, we first discuss the structure of the simulation in the *CMTJ* and its driver systems. Then we present some of the more advanced simulations where *CMTJ* provides valuable information, showing its ability to verify experimental setups that include, but are not limited to, static and dynamic characteristics of spin valves or magnetic tunnel junctions (MTJ).

RESULTS

Simulation design

The core of *CMTJ* is based on the Landau–Lifschitz–Gilbert–Slonczewski (LLGS) macrospin equation implemented in C++, with a simple header-only library interface. If the user wishes to benefit from the provided PYTHON interface, the setup involves a standard PIP installation process. The scope of the PYTHON interface covers all basic functionalities of the C++ core library, exposing the functions using the open-source solution PYBIND11²⁰. In addition, the PYTHON package offers utility functions that complement frequently used operations such as unit conversions, parallelism, parameter sweep, filtering, energy and resistance calculations, or template procedures for spin-diode ferromagnetic resonance (SD-FMR) or pulse-induced microwave magnetometry (PIMM). The library is composed of a couple of classes, mainly the *Junction* and *Layer* classes that define a basic magnetic component in the MTJ simulation and the *Driver* class that contains definitions of various excitations that influence the magnetisation dynamics of the system. We briefly discuss them in the following paragraphs, but detailed descriptions of key *CMTJ* functionality, as well as implementation details, can be found in the library documentation (<https://lemurpwned.github.io/cmtj/>).

The input to each simulation is the programmatic description of the system and its dynamic stimuli, which may vary over the simulation runtime. The result of a simulation holds the evolution

¹Institute of Electronics, AGH University of Science and Technology, Al. Mickiewicza 30, Kraków 30-059, Poland. ²Faculty of Physics and Applied Computer Science, AGH University of Science and Technology, Al. Mickiewicza 30, Kraków 30-059, Poland. ✉email: mojsiejuk@agh.edu.pl; zietek@agh.edu.pl

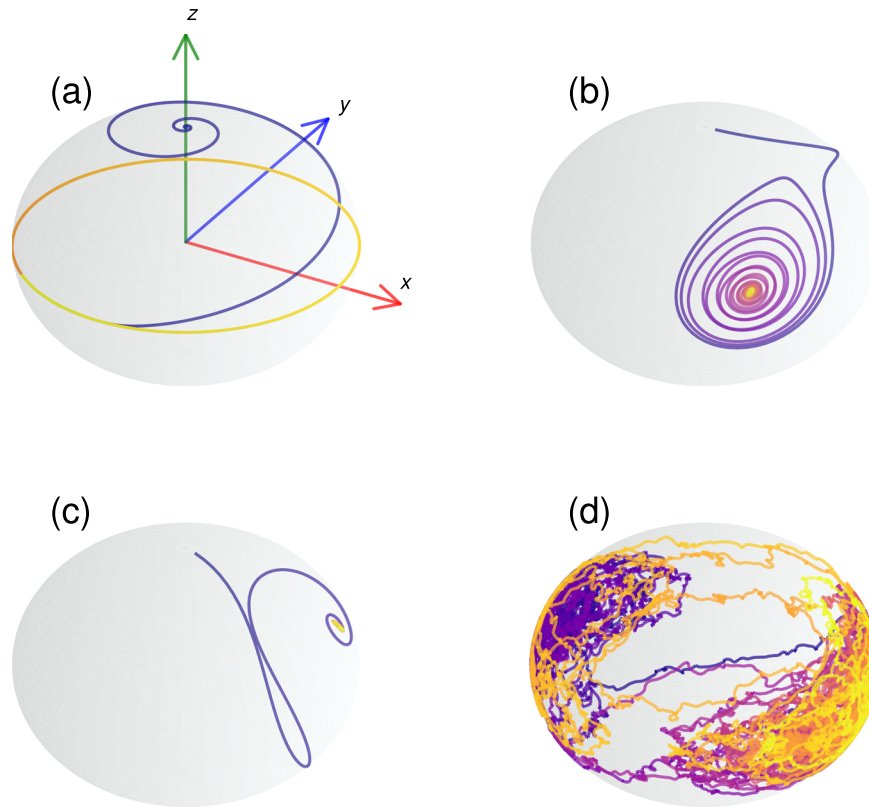


Fig. 1 Example trajectories extracted by simulating a single ferromagnetic layer with different parameters and excitations. **a** Depicts a stable oscillator trajectory under a constant current density. **b** Demonstrates a trajectory obtained with exciting the magnetisation with VCMA. In **c** we see a trajectory under a pulse excitation of the Oersted field. Finally, **d** is a thin, bilayer ferromagnetic system with a low-energy barrier that changes states from parallel to anti-parallel under thermal noise.

of the magnetisation vector for each layer at each time step, and if the user chooses so, additional time-dependent metadata such as different flavours of magnetoresistance²¹ or field contributions. All simulations in *CMTJ* are conceptually divided into three levels of abstraction: single-layer simulations, multilayer simulations, and stacked device simulations. The first of those levels are designed to provide a basic interface of the ferromagnetic (FM) layer, which is represented by a time-dependent magnetisation vector, as dictated by a macrospin model. Layers in *CMTJ* are created using the *Layer* class, for example:

```
# define the tensor using cmtj C++ binding class called CVector
demagTensor = [
    CVector(0.0002, 2.7139e-10, 5.9550e-14),
    CVector(2.7139e-10, 0.0001, 1.3250e-14),
    CVector(5.95503e-14, 1.3250e-14, 0.9995)
]
# create a simple layer
free_layer = Layer(
    id="free",
    mag=CVector(0, 0, 1),
    anis=CVector(0, 0., 1),
    Ms=1.6,
    thickness=2e-9,
    cellSurface=surface,
    damping=5e-3,
    demagTensor=demagTensor,
)
```

which defines a layer that can be later referred to by its 'free' id, with perpendicular anisotropy axis, initial magnetisation along the z-axis, magnetisation saturation, M_s , of 1.6 T, the thickness of 2 nm, Gilbert damping constant of $\alpha_G = 0.005$ and a demagnetisation tensor under variable name *demagTensor* (see the "Methods"

section for an explanation how those parameters influence the simulation). Multilayer simulation applications revolve most commonly around simple bilayer structures consisting of heavy metal (HM) and FM layers, or MTJs composed of FM layers, each separated by a thin tunnel barrier (TB). Non-ferromagnetic layers, such as HM, are not simulated in the package, but their inclusion in the experiment has direct consequences in the simulation. For example, between two FM layers separated by TB, there is an interlayer exchange coupling (IEC) that varies with thickness^{22,23}. Similarly, layers can be coupled in the multilayer system via a longer-range dipole interaction. HMs are typically simulated indirectly with the addition of STT or SOT terms^{24,25}. It is also possible to save computing time by including pinned layers, experimentally obtained by the exchange-bias structure enforced by the presence of an antiferromagnet. In such a case, the solver is not run for a pinned/reference layer, but the effects of SOT or STT are still modelled via a constant reference vector.

To create a multilayer device in *CMTJ*, the user needs to create at least one FM layer. Layers are then composed into a single *Junction* that represents a discrete multilayer system. A two-layer *Junction* can be defined as follows:

```
# Create MTJ composed of two FM layers created earlier
# Rap - anti-parallel, Rp - parallel resistance
mtj=Junction([free_layer, reference_layer],
    Rp=100, Rap=200)
```

Wrapping multiple layers into a single object provides an additional level of control; for instance, the same magnetic field or excitation may be applied to all members of the *Junction* with a single function instead of to each layer individually.

For some simulations, two or more junctions can be combined into a *Stack* of type *Parallel* or *Series*, which alters the resistance calculation. However, the main consequence of composing a *Stack*

device is the electrical coupling by a current passing through. The model for this kind of coupling follows the work of Taniguchi et al.²⁶. For a parallel or series stack of two junctions, the current depends on the free magnetisations \mathbf{m} and the pinning layers \mathbf{p} of the junctions i and $i + 1$:

$$I(t) = I_0(t) + \chi I_0(t)(\mathbf{m}_i \cdot \mathbf{p}_i + \mathbf{m}_{i+1} \cdot \mathbf{p}_{i+1}) \quad (\text{series}) \quad (1)$$

$$I(t) = I_0(t) + \chi I_0(t)(\mathbf{m}_i \cdot \mathbf{p}_i - \mathbf{m}_{i+1} \cdot \mathbf{p}_{i+1}) \quad (\text{parallel}) \quad (2)$$

where $I_0(t)$ represents the value of the uncoupled current. The coupling strength χ can be positive or negative, most of the time strictly much < 1 in absolute value. Creating a stack is simple; for example, setting a current density of $I_0 = 60 \text{ GA/m}^2$ through the stack with the coupling strength of 0.1 reduces to the following:

```
# create a parallel connection of junction1 and junction 1
stack=ParallelStack([junction1, junction2])
# set the constant current density fed into the system
stack.setCoupledCurrentDriver(ScalarDriver(
    getConstantDriver(6e10)))
# set coupling strength
stack.setCouplingStrength(0.1)
```

Excitation drivers

The dynamic pathway to excite any system in CMTJ takes place through the driver system. The user can define any excitation in the form of a driver, an adequate *Scalar* driver, or a vector (*Axial*) driver. The latter are just compositions of the former along each dimension (the x , y , and z axes independently). Each driver component is calculated at each time step and influences the selected effective field contributions. For instance, one may define a sinusoidal driver and use it as a driving excitation of the anisotropy, leading to stimulation of the VCMA effect:

```
# Junction called mtj was created earlier
# reference the free layer from 'mtj' using the Junction interface,
mtj.setLayerAnisotropyDriver("free",
    # arguments for the anisotropy sine driver are:
    # offset (J/m^3), amplitude (J/m^3), frequency (GHz), phase
    ScalarDriver.getSineDriver(
        K1, 1e3, 7e9, 0
    ))
```

Similarly, an externally applied magnetic field can be added through the *AxialDriver* class by specifying field contributions along each axis. For example, setting a constant field of 5 kA m^{-1} along the y -axis can happen by using a simple function call:

```
# reference all layers in the junction
mtj.setLayerExternalFieldDriver("all",
    AxialDriver(
        NullDriver(), # x, does nothing
        ScalarDriver.getConstantDriver(
            5e3), # y,
        NullDriver())) # z, does nothing
```

All mechanisms described in this section offer great flexibility in designing an experiment. Since drivers act as input to a state machine, the simulation may be paused, modified, and resumed without having to restart. The output is saved online in a native PYTHON dictionary object that assumes seamless integration with other common numerical, plotting, or machine-learning packages available in that language.

In the consecutive sections section, we focus on reproducing selected interesting experiments and, where possible, comparing the simulation result with the experimental data and analytical functions. The examples are arranged by the level of complexity, starting from the simplest towards more advanced ones. We decided to showcase the following techniques: standard $M(H)$ and $R(H)$ loops in the section " $M(H)$ and $R(H)$ loops", magnetoresistance (MR) based SD-FMR and PIMM in the section "Spin valve dynamics", harmonic Hall voltage detection, an angular variant

in the section "Angular harmonic Hall detection", current-induced magnetisation switching (CIMS) in Sect. "CIMS", electrical coupling of two MTJs in the section "Electrical coupling". These examples can be reproduced by running the JUPYTER notebooks from the GITHUB repository of the CMTJ package.

$M(H)$ and $R(H)$ loops

The $M(H)$ and $R(H)$ are the basic magnetic characterisation methods that allow the determination of various material parameters of the multilayer system, such as magnetisation saturation, magnetic anisotropy, or magnetoresistance ratio. The $M(H)$ loop simulates magnetometry measurements, such as a vibrating sample magnetometer (VSM) or magneto-optical Kerr effect (MOKE), whereas the $R(H)$ loops are indispensable in adjusting the magnetoresistance magnitude. By performing angular sweep simulations in different planes, one can also determine a type of magnetoresistance, because anisotropic MR (AMR), anomalous Hall effect MR (AHE), giant MR (GMR)/tunnelling MR (TMR) and spin-Hall MR (SMR) are characterised by different angular dependencies^{21,27,28}. Other magnetoresistance flavours, such as those presented, for example, in the works by Avci et al. and Vélez et al.^{29,30}, may be easily added after the magnetisation dynamics have been computed by CMTJ.

In the case of $M(H)$ and $R(H)$ loop simulation, we replicated the experimental method by extending the simulation time and collecting the magnetisation or resistance vector at the steady state for each magnitude of the swept magnetic field. As an example, magnetic-field-dependent simulations of the Co(4 nm)/Ru(0.65 nm)/Co(4 nm) system are presented in Fig. 2a–f. The data for this example come from, yet unpublished, wider research on the Co/Ru/Co trilayers. A similar setup may be found in ref.³¹. In the simulations, increasing H along the y direction leads to a scissor-shaped magnetisation vector alignment, which saturates at around 600 kA m^{-1} . This becomes particularly clear in the loop $M(H)$ for m_y component illustrated in Fig. 2b, with the remaining m_x and m_z having very small amplitudes. Furthermore, the simulation reveals that, due to antiferromagnetic coupling (AFM), the two layers oscillate in antiphase in a certain region, as depicted in Fig. 3. The experimental points for this sample were collected from SD-FMR measurement, with an external field applied at 45° angle respective to the long axis of the stripe, and an RF signal power of 16 dBm. The DC voltage originating from the mixing between oscillating resistance and the in-phase current

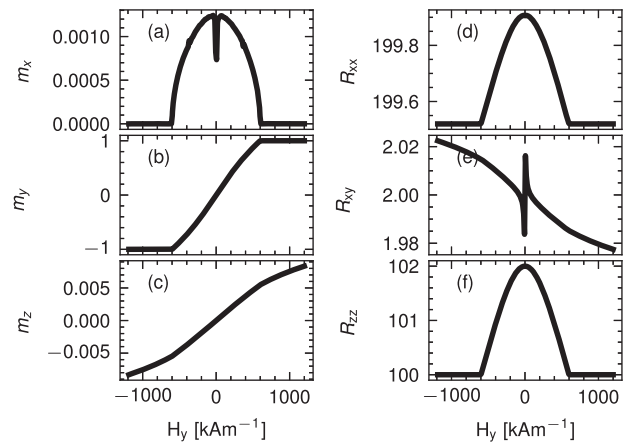


Fig. 2 Steady-state simulations of the Co/Ru/Co system with the transverse applied field. $M(H)$ a–c and $R(H)$ d–f loops simulated with parameters taken from Supplementary Table 1. The magnetic moment is normalised to unity, whereas the SMR, AMR, and GMR magnitudes are set to -0.24 , -0.045 , and 2Ω , respectively (note that m_y and m_z components show very little variation with the applied field).

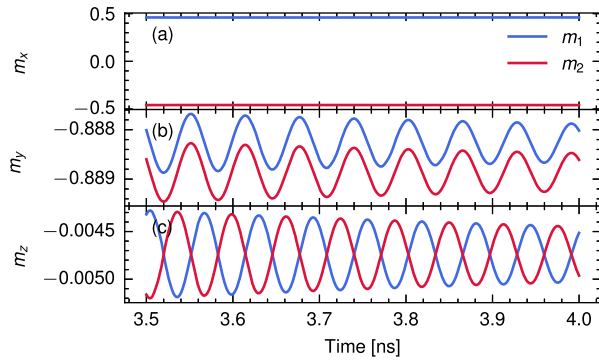


Fig. 3 Co(4 nm)/Ru(0.65 nm)/Co(4 nm) system with both linear and quadratic components of the IEC. **a–c** magnetisation trajectory components for a $H_{\text{ext}} = 513 \text{ kA m}^{-1}$, marked with the dashed white line in **(d)**. Colour denotes a layer, blue for the top and red for the bottom layer. **c** Shows that the m_z components of the two layers oscillate in antiphase. **d** Kittel dispersion relation obtained from PIMM (described in the section “Spin valve dynamics”), with experimental points from SD-FMR (given by blue dots), and phase difference $\Delta\phi_z$ between m_z components of two layers (solid white line) across the external magnetic field range. The region between approximately -600 and 600 kA m^{-1} , where the optical branch is visible, exhibits antiphase oscillation of m_z components. Parameters are taken from Supplementary Table 1.

was obtained using Hall-bar system by a lock-in amplifier synchronised to an amplitude-modulated RF source.

Spin valve dynamics

A more complex example begins with a study of a CoFe(2.1 nm)/Cu(1.9–2.37 nm)/CoFe(1 nm)/NiFe(5 nm) spin valve sample with variable thickness of the Cu spacer layer. This system exhibits characteristic oscillatory coupling varying with spacer thickness, which is well described in terms of the Rudermann–Kittel–Kasuya–Yosida (RKKY) interaction between the magnetisations of the reference and the free layers³². Resulting GMR, $R(\theta)$, is calculated with respect to resistances in parallel (R_P) and antiparallel states (R_{AP}):

$$R(\theta) = R_P + \frac{1}{2}(R_{AP} - R_P)(1 - \mathbf{m}_{\text{free}} \cdot \mathbf{m}_{\text{reference}}) \quad (3)$$

where θ is the angle between the magnetisation vectors of the free and reference layer, \mathbf{m}_{free} is the magnetisation of the free layer, and $\mathbf{m}_{\text{reference}}$ is the magnetisation of the reference layer. Using the parameters for the system from the papers^{32,33}, also summarised in Supplementary Table 2, we perform SD-FMR and PIMM simulations.

Experimentally SD-FMR methods involve supplying AC current, I_{AC} , in a given frequency range, typically between 2 and 40 GHz, while sweeping with an external magnetic field. As a result, the DC mixing voltage V_{mix} arises, which is essentially a function of both the frequency and the magnitude of the external magnetic field³⁴. Thus, SD-FMR allows for the calculation of the ferromagnetic resonance frequency for a given set of system parameters in the form of a Kittel dispersion relation. Furthermore, analysis of the shape of the simulated signal can be used to determine the spin torque values, in the current perpendicular to the plane STT³⁵ and in-plane SOT geometries²⁴. In the simulation setup, a representation of SD-FMR is modelled with a 2D map, where V_{mix} , the mixing voltage of $R(\theta)$ and I_{AC} at a frequency f , is plotted against a range of applied external field, H . For each field and frequency, the I_{AC} time series is multiplied by a magnetoresistance time series and then passed through a low-pass filter. Finally, the mixing voltage is extracted as a means of that signal. The results are presented in Fig. 4 with bright green hollow circles as experimental points for comparison. In simple cases, a known analytical relation, in the form of the Kittel dispersion function³⁶, produces the main resonance mode of the system:

$$f = \frac{\gamma_e}{2\pi} \sqrt{B(B + \mu_0 M_s)} \quad (4)$$

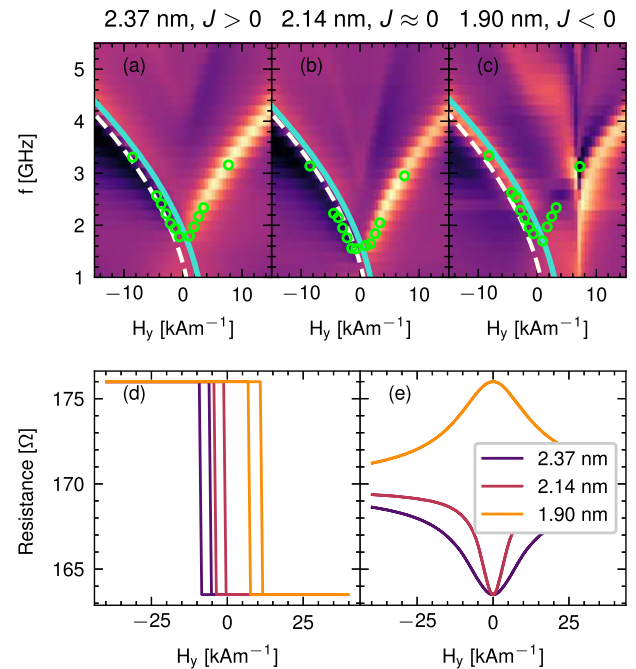
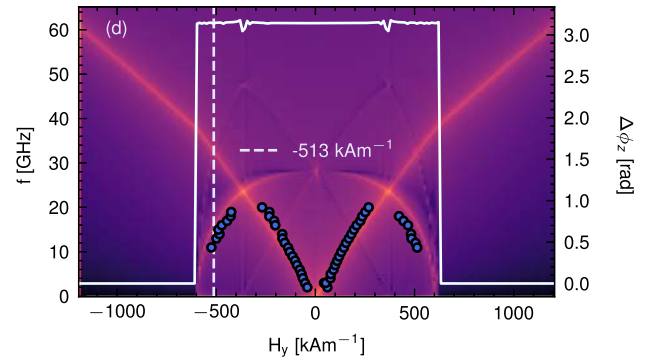


Fig. 4 Spin valve simulations of CoFe(2.1 nm)/Cu(1.9–2.37 nm)/CoFe(1 nm)/NiFe(5 nm) sample for three different values of Cu thickness which result in different IEC magnitudes. **a–c** Kittel dispersion relations, with the blue dots marking the experimental data. Resistance loops at $\phi_H = 90^\circ$ **(d)** and at $\phi_H = 0^\circ$ **(e)** applied external magnetic field with ϕ denoting the polar angle. Solid turquoise lines mark the fit to Kittel's formula, Eq. (4) and ivory dashed line represents simulated data from the free-energy Smit–Beljers model. Discrepancies between Kittel and Smit–Beljers model may come from the fact that the latter is better suited to multilayer systems. Parameters of the system may be found in Supplementary Table 2.

where the $\frac{\gamma_e}{2\pi}$ factor is $\approx 28,024 \text{ MHz T}^{-1}$, and the B field is composed of an external magnetic field, an interlayer exchange coupling field, and an anisotropy field, respectively: $B = \mu_0(H_{\text{ext}} + H_{\text{IEC}} + H_K)$ (see the section “Field contributions” for more details on how they are computed macro magnetically). We plot the fit to Eq. (4) in Fig. 4 with the solid turquoise line. In addition to Kittel's model, we included the free-energy model

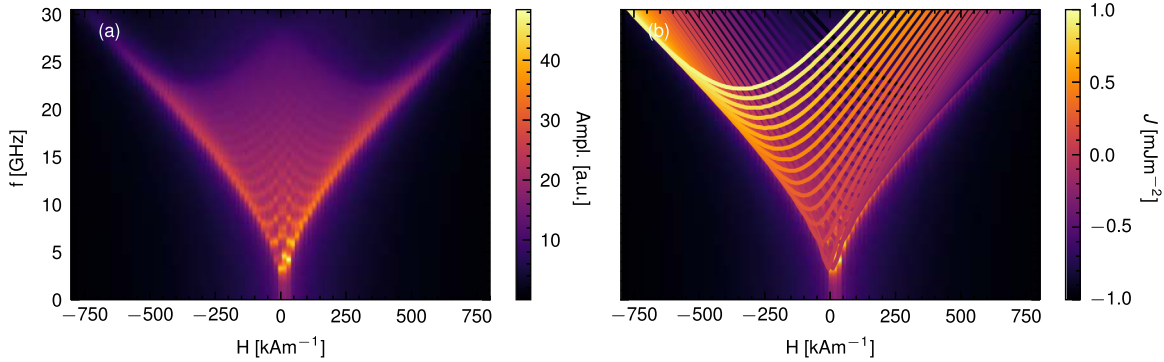


Fig. 5 PIMM scans of the CoFe(2.1 nm)/Cu(1.9–2.37 nm)/CoFe(1 nm)/NiFe(5 nm) system in the function of IEC constant J_{linear} . **a** spectrum of multiple IEC values in $(-1, 1 \text{ mJ m}^{-2})$ was combined into a single map. The colour indicates the total frequency amplitude summed over all PIMM simulations. **b** Illustrates the same PIMM, but with a marked maximum amplitude resonance line for each J_{linear} value mapped accordingly to the colour scale. The colour scale attached represents different IEC values, from -1 to 1 mJ m^{-2} . We observe the shift of the resonance curve towards the centre for smaller absolute IEC values. Note that at $H = 0$ the system still exhibits non-zero oscillation. Parameters used for simulation can be found in Supplementary Table 2. Field applied along at 45° angle between x and y axes.

based on the Smit–Beljers model³⁷ (dashed ivory line), which yields more precise results for a multilayer case. The key effect modelled in Fig. 4a–c is the increase of the zero-field oscillation frequency when the IEC increases with absolute value. In Fig. 4d the simulation captures the shift of the resistance loop at $\phi_H = 90^\circ$ and the widening of the resistance curve peak at $\phi_H = 45^\circ$ in Fig. 4e, all respectively, for the case where $J \approx 0$. In any case, macromagnetic simulation, being a dynamic process, can model the experimental data more accurately for that particular experiment. A further advantage of computing the dynamics is that we obtain the full SD-FMR map, rather than the individual resonance modes, as is the case with the Smit–Beljers model.

Apart from the SD-FMR method described above, magnetisation dynamics can also be investigated by analysing the magnetisation response to picosecond magnetic field pulses. In the experiment, this time domain method is performed indirectly using PIMM^{38–40}. From the simulation perspective, PIMM is simulated as an analysis of the free oscillations induced by a short magnetic field pulse, contrary to the dynamics caused by the alternating signal input, as is the case for the FMR. Specifically, we measure the response to a step excitation of a short-lived (2–3 ps), small-amplitude (usually about 50–100 Oe) Oersted field pulse along the z -axis. This corresponds to the experimental setup where a short DC pulse is injected into the system. If the FFT computation of the pulse response for each value of the applied magnetic field from the sweep is repeated, one can obtain a spectrogram representing the dispersion relation, where each pixel denotes the FFT magnitude for a given frequency and magnetic field. For the spin valve system, multiple PIMM simulations are performed for a range of different IEC values and then overlaid, resulting in Fig. 5a, b. Similarly as in the case of the SD-FMR experiment, when the magnitude of the IEC coupling increases, the resonance curve shifts away from the zero fields.

Angular harmonic Hall voltage detection

There are several experimental methods that lead to the determination of the SOT components: SOT-FMR line⁴¹ and line width analysis⁴², the SOT switching current analysis⁴³, or field-dependent harmonic Hall voltage techniques⁴⁴. Another approach, less susceptible to various artefacts, such as the anomalous Nernst effect, is called the angular harmonic Hall voltage⁴⁵. Our model has been thoroughly verified using the field-dependent method⁴⁶, here we present a simplified angular variation of the harmonic Hall voltage detection. The standard

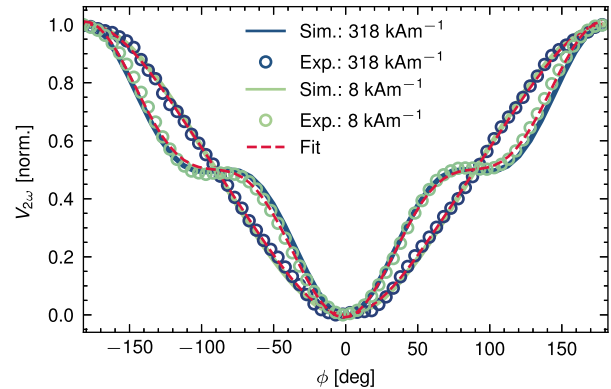


Fig. 6 Second Harmonic Hall voltage detection in angular variation. Hollow dots represent the experiment, solid lines mark the simulation data and a dashed red line denotes the fit to Eq. (5). The y -axis is normalised. Measurement data was collected from Pt(4.3 nm)/FeCoB(2 nm) device, for two example magnitudes of the external magnetic field.

process for obtaining torque amplitudes $H_{\text{DL/FL}}$ in the angular variation of harmonic Hall voltage detection follows the model of Avci et al.^{47,48}:

$$V_{2\omega} = \left(-\frac{H_{\text{FL}}}{H_{\text{ext}}} V_P \cos 2\phi - \frac{1}{2} \frac{H_{\text{DL}}}{H_{\text{eff}}} V_A + V_{\text{ANE}} \right) \cos \phi \quad (5)$$

where ϕ is the angle in the plane between the long axis of the Hall bar and magnetisation. The effective field H_{eff} includes the external field H_{ext} and the anisotropy field, H_K . V_P and V_A are the planar and anomalous Hall voltages, respectively. V_{ANE} is a contribution of the anomalous Nernst effect. We show the simulation result, along with the experimental results for the corresponding Pt(4.3 nm)/FeCoB(2 nm) sample⁴⁹, in Fig. 6. Each line is produced by sweeping with the azimuth angle $\phi \in [-180^\circ, 180^\circ]$ at the frequency f of the AC current and measuring the second harmonic output in the mixing voltage of the input current (for details of the experimental setup, see ref. 49). The parameters for this system can be found in Supplementary Table 3. The signal consists of one part proportional to the damping-like field with a $\cos \phi \cos 2\phi$ dependence and another, related to the field-like term. The former dominates in small magnetic fields because it is scaled by an external field alone, unlike the latter, which is scaled by the effective field (which also includes anisotropy and

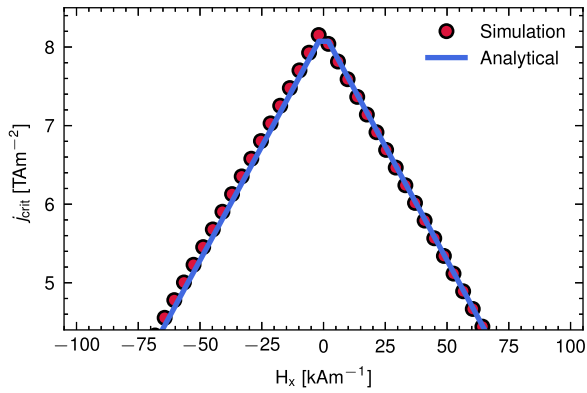


Fig. 7 Critical switching current densities as a function of external field H_x for Pt(4 nm)/Co(1 nm)/MgO SOT device. Fit to analytical formula is represented as a solid blue line and red dots depict the simulated result.

demagnetising fields). In Fig. 6, this torque causes an inflexion in the curve at large ϕ angles.

CIMS

Next, we discuss an example of SOT-induced magnetisation switching in the HM/FM bilayer. The experimental data were obtained in the multilayer system: Pt(4 nm)/Co(1 nm)/MgO (A1) from the work of Grochot et al.⁵⁰. In this case, we reproduce the theoretical switching behaviour of the system using the field-like and damping-like SOT, and magnetic parameters obtained from the experiment. The result is shown in Fig. 7. We approximated the critical current density analytically using a formula from Lee et al.⁵¹:

$$j_{sw} \approx \frac{2e\mu_0 M_s t_{FM}}{\hbar \theta_{SH}} \left(\frac{H_K}{2} - \frac{H_x}{\sqrt{2}} \right) \quad (6)$$

where e is the electron charge, μ_0 is the magnetic permeability in a vacuum, M_s is the magnetisation saturation, \hbar is the reduced Planck constant, θ_{SH} is the effective spin Hall angle, H_K is the effective perpendicular anisotropy value, and H_x is the applied field along the x direction.

For simulations, we used the trapezoidal impulse shape, with a rising and falling edge of 1 ns and a flat edge of 3 ns. We also normalised the damping- and field-like torque magnitudes obtained from the experiment by the current density with which they were measured. Under the current density sweep, they will scale proportionally, giving the correct values of H_{DL} and H_{FL} at each step.

Electrical coupling

Using this example, we illustrate how electric coupling can be simulated with CMTJ. First, we created two MTJs with slightly different magnetic and resistance parameters, emulating a typical experimental dispersion. Then, using the interface of the *Stack* class (see the section “Simulation design”), we couple them in a parallel connection, setting the coupling value χ . We sweep the external magnetic field at the azimuthal angle of 5° and measure the frequency response of the stack to constant current density excitation. For larger values of the applied external magnetic field and negative coupling constant χ , we observe how two main resonance lines, each corresponding to a separate MTJ, converge towards a common resonance mode. Ultimately, around 250 kA m^{-1} , the two MTJs desynchronise and their resonance lines separate again. The result of the electric synchronisation of two MTJs is depicted in Fig. 8a, while Fig. 8b and c illustrate a situation with a positive coupling coefficient and coupling disabled, respectively. This example shows that the software

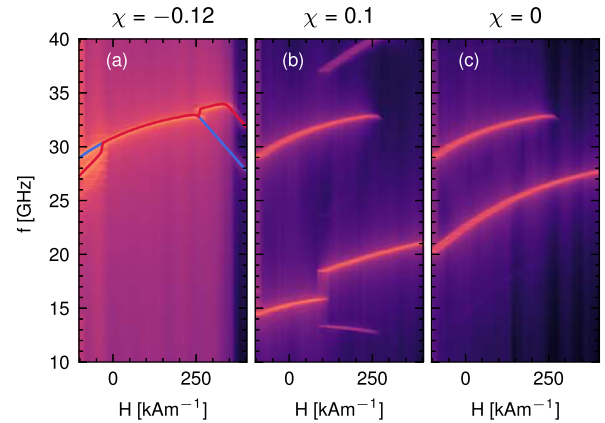


Fig. 8 The electric synchronisation of two MTJs. Electric coupling constant was set to $\chi = -0.12$ (a) and $\chi = 0.1$ (b). Solid blue and red lines in (a) indicate the primary resonance modes of individual MTJs from the stack. c Shows the same device with no coupling present.

presented can also be used in more complex systems, for example, for the analysis of neural computing platforms⁵². The parameters of the coupled system have been collected in Supplementary Table 4.

DISCUSSION

In this article, we presented CMTJ, fast modelling software for macrospin simulation of magnetic heterostructures. Its core is grounded in the LLGS equation, and the package is capable of calculating both the static and dynamic characteristics of spintronic devices. However, macrospin simulations are inherently limited in modelling any sort of spin wave or materials with non-uniform magnetisation and therefore are not a suitable method in cases where those effects play a key role. Yet, many experimental setups in electrical detection are, in principle, averaged pictures of reality. For instance, in measurements such as $M(H)$ or $R(H)$, we observe only a mean value of multi-domain behaviour of magnetisation or resistance. Therefore, in such use cases, the use of macrospin modelling can be justified and, as shown in the previous sections, results obtained from CMTJ agree well with the experimental data.

The key benefit of using macrospin over micromagnetic frameworks is the speed of computation. Additionally, with the Python bindings CMTJ provides, the package can be used directly in common parameter search procedures that involve Bayesian optimisation processes or neural network training. The combination of those two advantages, performance and integration with native Python code, hints at the intended use of CMTJ, which lies in large-scale sweeps over multidimensional parameter spaces. Such an application plays an interesting role in understanding how different magnetic parameters influence the dynamics of the spintronic device.

Finally, in the spirit of the modern modular development approach suggested, for example, in refs. ^{53,54}, CMTJ expands its usability to connect multiple spintronic structures using the *Junction* or *Stack* system. Future extensions based on the modular approach may involve the addition of a separate structure, such as a reservoir, where an array of thin-layer spintronics devices is dynamically coupled through dipole interaction^{55,56}.

METHODS

Magnetisation dynamics

The pivotal equation for magnetic macrospin simulations is called Landau–Lifshitz–Gilbert–Slonczewski (LLGS)^{15,45,57–59}. In the

simulation, we use the numerically solvable LL-form of that equation. A formulation with SOT torques included in the package has the following form:

$$\frac{d\mathbf{m}}{dt} = \frac{-\gamma_0}{1+\alpha_G^2} [\mathbf{m} \times \mathbf{H}_{\text{eff}} + \alpha_G \mathbf{m} \times \mathbf{m} \times \mathbf{H}_{\text{eff}}] + \frac{-\gamma_0}{1+\alpha_G^2} [\mathbf{m} \times \mathbf{p}(H_{\text{FL}} - \alpha_G H_{\text{DL}}) + \mathbf{m} \times \mathbf{m} \times \mathbf{p}(H_{\text{DL}} + \alpha_G H_{\text{FL}})] \quad (7)$$

where $\mathbf{m} = \frac{\mathbf{M}}{M_s}$ is a normalised magnetisation vector, with M_s as the magnetisation saturation, \mathbf{H}_{eff} as the effective field, α_G as the dimensionless Gilbert damping parameter, \mathbf{p} is the polarisation vector, and γ_0 is the gyromagnetic factor. Factors H_{DL} and H_{FL} are the so-called damping and field-like torque amplitudes, respectively. Usually, for small values of α_G , compared to the torque value, the torque mixing can be omitted in the last two terms in this form of the equation.

For structures where the spin current is injected through HM, the values of the SOT torques are usually taken from the experiment. For example, in the harmonic Hall voltage measurement⁴⁵, their values can be computed with the following equation:

$$H_{\text{DL}} = -\frac{2\rho_L \pm 2\kappa\rho_T}{\zeta} \frac{1}{1-4\kappa^2} \quad (8)$$

where κ is the ratio of the planar Hall effect and the resistance of the anomalous Hall effect and $\rho_{L/T} = \partial V_{2\omega} / \partial H_{\text{ext}}^{L/T}$ for the longitudinal arrangement L, when an external magnetic field is applied along the length of the sample, and the transverse arrangement T, when the field is applied along the width of the sample. The parameter $\zeta = \partial^2 V_{\omega} / \partial H_{\text{ext}}^2$ is obtained by fitting the low-field regime of the first harmonic response, V_{ω} to a quadratic function. Substituting the subscripts L and T produces torque H_{FL} . The voltage in the experiment arises as a response to the low-frequency AC current in longitudinal and transverse arrangements, but in the simulations, we often model it as an Oersted field excitation along the y direction. More details can be found in ref. ⁴⁶. For simulations more suited to the STT model, we assume the following LL form of the LLGS equation:

$$\frac{d\mathbf{m}}{dt} = \frac{-\gamma_0}{1+\alpha_G^2} [\mathbf{m} \times \mathbf{H}_{\text{eff}} + \alpha_G \mathbf{m} \times \mathbf{m} \times \mathbf{H}_{\text{eff}}] + \frac{-\gamma_0}{1+\alpha_G^2} [a_j \epsilon \beta (\mathbf{m} \times \mathbf{p}) + a_j \epsilon (\mathbf{m} \times \mathbf{m} \times \mathbf{p})] \quad (9)$$

with β as the secondary parameter that describes the torque (usually set to 0 or equal to the damping parameter α_G). The variable a_j is defined in terms of current density j :

$$a_j = \frac{\hbar j}{e M_s t_{\text{FM}}} \quad (10)$$

where \hbar is the reduced Planck constant and e is the electron charge. Furthermore, the variable ϵ depends on λ , the parameter of the spacer layer derived by Slonczewski, and η , the efficiency of the spin current polarisation ($0 \leq \eta \leq 1$):

$$\epsilon = \frac{\eta \lambda^2}{\lambda^2 + 1 + (\lambda^2 - 1) \mathbf{m} \cdot \mathbf{p}} \quad (11)$$

Often, λ is set to 1, which consequently removes the dependence of torque magnitudes on $\mathbf{m} \cdot \mathbf{p}$.

Field contributions

In this section, we describe in detail the methods for computing field contributions. The effective field vector \mathbf{H}_{eff} is usually composed of various field contributions that, depending on the context of the simulation, may be added or disabled. CMTJ provides a range of such contributions:

$$\mathbf{H}_{\text{eff}} = \mathbf{H}_{\text{ext}} + \mathbf{H}_{\text{IEC}} + \mathbf{H}_{\text{Oe}} + \mathbf{H}_{\text{K}} + \mathbf{H}_{\text{demag}} + \mathbf{H}_{\text{dipole}} + \mathbf{H}_{\text{th}}^* + \mathbf{H}_{1/f}^* \quad (12)$$

where each component corresponds, respectively, to the applied external field, interlayer exchange coupling (IEC), Oersted field, anisotropy field, demagnetising, dipole, thermal, and 1/f noise field⁶⁰ (all expressed in A m^{-1}). Contributions marked with * require a stochastic solver. Each of the contributions that constitute \mathbf{H}_{eff} may be varied over time using a driver system, as laid out in the section “Excitation drivers”.

Anisotropy field. In CMTJ, the anisotropy contribution has two parameters—the axis \mathbf{a} which determines a uniaxial anisotropy vector and the scalar value K_u which determines the amplitude of the anisotropy field. The axis parameter is passed in the layer constructor function. However, the scalar value can be driven dynamically using a *Driver* mechanism using the *Layer* or *Junction* API. The formula we use in CMTJ is as follows:

$$\mathbf{H}_{\text{K}} = \frac{2K_u}{\mu_0 M_s} (\mathbf{m} \cdot \mathbf{a}) \mathbf{a} \quad (13)$$

Interlayer exchange coupling field. The interlayer exchange coupling governs the RKKY-like interaction between neighbouring FM layers separated by a metallic spacer⁶¹. In CMTJ we include both linear (J_{linear}) and quadratic (J_{quad}) contributions. The contribution enters the effective field of layer i as a result of the interaction with layer j in the form:

$$\mathbf{H}_{\text{IEC},i} = \frac{1}{\mu_0 M_s t_{\text{FM}}} [J_{\text{linear}} \mathbf{m}_j + 2J_{\text{quad}} (\mathbf{m}_i \cdot \mathbf{m}_j) \mathbf{m}_j] \quad (14)$$

If a given FM layer is sandwiched between two other FM layers, then the engine will compute the IEC contribution from the top and bottom layers separately and then add them both to the effective field.

Demagnetisation and dipole fields. The demagnetisation interaction has a source in the geometry of the sample. On the other hand, the dipole interaction is a long-range interaction that originates from coupling with other FM layers. Both demagnetisation and dipole fields can be calculated from the tool linked in the repository CMTJ (<https://github.com/pawelkulig1/Demagnetization-Tensor-Tool>). The tool computes a dipole and demagnetising tensor based on the finite difference method and analytical calculations derived in refs. ^{62–64}. These tensors can be set directly in the simulation. Specifically, the demagnetisation tensor is passed through the constructor of a *Layer*. The dipole is set using *setBottomDipoleTensor* if the interaction originates from the top layers relative to the current layers or *setTopDipoleTensor* if the dipole interaction originates from the FM layers underneath. The field contribution of dipole and demagnetisation hence takes the form:

$$\mathbf{H}_{\text{dipole/demag}} = -M_s \mathbf{N} \mathbf{m} \quad (15)$$

where \mathbf{N} is the dipole or demagnetisation tensor and \mathbf{m} is the magnetisation of the current layer (demagnetisation) or the coupled layer (dipole). Often the demagnetisation tensor may be approximated by its diagonal when the off-diagonal terms become negligible compared to the diagonal ones.

Oersted field. The Oersted field is statically modelled in CMTJ, which means that users can dynamically change it during simulation, but it is not precomputed based on the input current. Obtaining a value of the Oersted field in an element may be a complicated problem. For simple FM/HM bilayer systems⁴¹, the Oersted field can be calculated from a simple relation: $H_{\text{Oe}} = j t_{\text{HM}} / 2$ where t_{HM} is the thickness of the HM. In more involved cases, numerical integration or variations of finite-difference methods are required to obtain a precise result.

Table 1. Example of serial execution times and the number of steps per experiment.

Benchmark	Steps [10^6]	Time [s]	Steps per s [10^3 per s]
M(H), R(H), PIMM	50	42	1190
CIMS	187.5	823	228
Spin valve VSD	1872	748	2503
Spin valve PIMM	360	315	1143
Stack synchronisation	120	62	1935

The number of steps summarises all sweeps over parameters, fields, frequencies, and the number of iterations during the simulation time. The timing was done on a MacBook Pro 2020 with an Apple M1 processor and 16 GB of RAM. Some experiments, such as, for instance, CIMS, involve more parameter scanning than individual simulation steps, so they are less efficient than simulations with longer in-simulation time, such as VSD for the spin valve system.

1/f field. The amplitude of the noise field $1/f$ is calculated using a modified Voss–McCartney–Trammel (VMT) algorithm⁶⁰. Being a stochastic contribution, it has the following form:

$$\mathbf{H}_{1/f} = c\eta_{\text{VMT}}d\mathbf{W}_t \quad (16)$$

where c is the scaling parameter, η_{VMT} is generated from the VMT algorithm, and $d\mathbf{W}_t$ is the random unit vector. The user specifies a number of generating sources k , and a Bernoulli distribution bias parameter p . At each generation step, k numbers are drawn from the Bernoulli distribution, each representing a source active in that step. For each unique index, a random float is generated, contributing to the total amplitude of the $1/f$ noise, η_{VMT} .

Solver methods

The core solver for most of the systems in *CMTJ* is the Runge–Kutta 4 (RK4) algorithm, as it balances decent convergence with speed. However, if the user specifies a temperature component for the system, *CMTJ* switches to the stochastic solver, using the Euler–Heun or Heun method, and solves the Stratonovich form of the LLG equation⁶⁵:

$$d\mathbf{m}(t) = \mathbf{f}(\mathbf{m}(t), t)\Delta t + \mathbf{g}(\mathbf{m}(t), t) \circ d\mathbf{W}_t \sqrt{\Delta t} \quad (17)$$

where the non-stochastic part $\mathbf{f}(\mathbf{m}(t), t)$ is the LL form of the LLG equation, while the stochastic part, $\mathbf{g}(\mathbf{m}(t), t)$ contains thermal and other stochastic contributions. Δt is the integration step of the numerical method. For example, in the Langevin thermal field, we have the following:

$$\mathbf{g}(\mathbf{m}_t, t) \circ d\mathbf{W}_t = -\frac{\sigma\gamma}{1+a^2} [\mathbf{m} \times d\mathbf{W}_t + a\mathbf{m} \times (\mathbf{m} \times d\mathbf{W}_t)] \quad (18)$$

where $d\mathbf{W}_t$ is the random unit vector whose components are sampled from the normal distribution with zero mean, $\mathcal{N}(0, 1)$, σ is the standard deviation of thermal noise^{66,67}. From our experience, an optimal integration time should be of the order of at least a picosecond, or tenths of a picosecond, for either type of solver, which was verified experimentally. In cases involving strong IEC coupling or larger stochastic excitation, even shorter integration times may be required. In cases involving strong IEC coupling or larger stochastic excitation, much lower integration times may be required.

Magnetoresistance

Apart from tunnelling and giant magnetoresistance, which are calculated as per Eq. (3), we also include methods to compute longitudinal R_{xx} and transverse R_{xy} magnetoresistance²¹,

expressed in terms of magnetisation vector components:

$$R_{xx} = R_{xx0} + (\Delta R_{\text{AMR}}m_x^2 + \Delta R_{\text{SMR}}m_y^2) \quad (19)$$

$$R_{xy} = R_{xy0} + \frac{1}{2}\Delta R_{\text{AHE}}m_z + \frac{w}{l}(\Delta R_{\text{SMR}} + \Delta R_{\text{AMR}})m_xm_y \quad (20)$$

where w and l are the width and length of the sample. ΔR_{SMR} , ΔR_{AMR} , ΔR_{AHE} are the magnitudes of the spin-Hall, anisotropic, and Anomalous Hall Effect resistances, respectively. R_{xx0} and R_{xy0} are base longitudinal and transverse resistances.

Benchmarks

The *CMTJ* is meant to run on personal computers as well. In Table 1 we present example execution times for more computationally challenging examples described in the sections “*M(H)* and *R(H)* loops, Spin valve dynamics, Angular harmonic Hall voltage detection, CIMS, and Electrical coupling”. The runtimes were recorded on a typical 2020 MacBook Pro with Apple Silicon M1 with 16 GB RAM. In the table, the step column designates the number of RK4 steps. For example, in the spin valve VSD experiment, we scan with a field for every frequency; therefore, the total number of steps is frequency steps \times field steps \times (simulation time/integration time). The measured times in Table 1 are given for a serial execution of each experiment. However, the *CMTJ* library also includes additional helper functions that allow for easy parallelism, designed for simulations performed across multiple parameter spaces.

DATA AVAILABILITY

The data supporting the findings of this study are available from the corresponding author on a reasonable request.

CODE AVAILABILITY

Code used in this work is open source and can be accessed free of charge under the following webpage <https://github.com/LemurPwned/cmtj> (the release version for this article is marked as 1.3.0). The examples section in the repository contains the code required to reproduce the results presented in this manuscript.

Received: 11 August 2022; Accepted: 16 March 2023;

Published online: 06 April 2023

REFERENCES

- Dieny, B. et al. Opportunities and challenges for spintronics in the microelectronics industry. *Nat. Electron.* **3**, 446–459 (2020).
- Ikegawa, S., Mancoff, F. B., Janesky, J. & Aggarwal, S. Magnetoresistive random access memory: present and future. *IEEE Trans. Electron Devices* **67**, 1407–1419 (2020).
- Xu, Y., Yang, Y., Luo, Z., Xu, B. & Wu, Y. Macro-spin modeling and experimental study of spin-orbit torque biased magnetic sensors. *J. Appl. Phys.* **122**, 193904 (2017).
- Hirohata, A. et al. Review on spintronics: principles and device applications. *J. Magn. Magn. Mater.* **509**, 166711 (2020).
- Vansteenkiste, A. et al. The design and verification of MuMax3. *AIP Adv.* **4**, 107133 (2014).
- Donahue, M. J. & Porter, D. G. *OOMMF User's Guide, Version 1.0* (National Institute of Standards and Technology (NIST), 1999). <https://doi.org/10.6028/NIST.IR.6376>.
- Kresse, G. & Hafner, J. Ab initio molecular dynamics for liquid metals. *Phys. Rev. B* **47**, 558–561 (1993).
- Giannozzi, P. et al. QUANTUM ESPRESSO: a modular and open-source software project for quantum simulations of materials. *J. Phys. Condens. Matter* **21**, 395502 (2009).
- Giannozzi, P. et al. Advanced capabilities for materials modelling with quantum ESPRESSO. *J. Phys. Condens. Matter* **29**, 465901 (2017).
- Evans, R. F. L. et al. Atomistic spin model simulations of magnetic nanomaterials. *J. Phys. Condens. Matter* **26**, 103202 (2014).

11. Müller, G. P. et al. *Spirit*: multifunctional framework for atomistic spin simulations. *Phys. Rev. B* **99**, 224414 (2019).
12. Garg, R., Kumar, D., Jindal, N., Negi, N. & Ahuja, C. Behavioural model of spin torque transfer magnetic tunnel junction, using Verilog-A. *Int. J. Adv. Res. Technol.* **1**, 36–42 (2012).
13. Chen, T. et al. Comprehensive and macrospin-based magnetic tunnel junction spin torque oscillator model—Part II: Verilog-A model implementation. *IEEE Trans. Electron Devices* **62**, 1045–1051 (2015).
14. Chen, T. et al. Comprehensive and macrospin-based magnetic tunnel junction spin torque oscillator model—Part I: analytical model of the MTJ STO. *IEEE Trans. Electron Devices* **62**, 1037–1044 (2015).
15. Slonczewski, J. Current-driven excitation of magnetic multilayers. *J. Magn. Magn. Mater.* **159**, L1–L7 (1996).
16. Ogorodnik, P. et al. Study of spin-orbit interactions and interlayer ferromagnetic coupling in Co/Pt/Co trilayers in a wide range of heavy-metal thickness. *ACS Appl. Mater. Interfaces* **13**, 47019–47032 (2021).
17. Kiselev, S. I. et al. Microwave oscillations of a nanomagnet driven by a spin-polarized current. *Nature* **425**, 380–383 (2003).
18. Myers, E. B., Ralph, D. C., Katine, J. A., Louie, R. N. & Buhrman, R. A. Current-induced switching of domains in magnetic multilayer devices. *Science* **285**, 867–870 (1999).
19. Nozaki, T. et al. Electric-field-induced ferromagnetic resonance excitation in an ultrathin ferromagnetic metal layer. *Nat. Phys.* **8**, 491 (2012).
20. Wenzel, J., Rhinlander, J. & Moldovan, D. pybind11 — Seamless operability between C++11 and Python. <https://github.com/pybind/pybind11> (2017).
21. Kim, J., Sheng, P., Takahashi, S., Mitani, S. & Hayashi, M. Spin Hall magnetoresistance in metallic bilayers. *Phys. Rev. Lett.* **116**, 097201 (2016).
22. Katayama, T. et al. Interlayer exchange coupling in Fe/MgO/Fe magnetic tunnel junctions. *Appl. Phys. Lett.* **89**, 112503 (2006).
23. Koziol-Rachwał, A. et al. Interlayer exchange coupling, dipolar coupling and magnetoresistance in Fe/MgO/Fe trilayers with a subnanometer MgO barrier. *J. Magn. Magn. Mater.* **424**, 189–193 (2017).
24. Liu, L. et al. Spin-torque switching with the giant spin Hall effect of tantalum. *Science* **336**, 555–558 (2012).
25. Miron, I. M. et al. Perpendicular switching of a single ferromagnetic layer induced by in-plane current injection. *Nature* **476**, 189–193 (2011).
26. Taniguchi, T., Tsunegi, S. & Kubota, H. Mutual synchronization of spin-torque oscillators consisting of perpendicularly magnetized free layers and in-plane magnetized pinned layers. *Appl. Phys. Express* **11**, 013005 (2018).
27. Cho, S., Baek, S.-h.C., Lee, K.-D., Jo, Y. & Park, B.-G. Large spin Hall magnetoresistance and its correlation to the spin-orbit torque in W/CoFeB/MgO structures. *Sci. Rep.* **5**, 14668 (2015).
28. Rzeszut, P., Skowroński, W., Ziętek, S., Ogorodnik, P. & Stobiecki, T. Biaxial magnetic-field setup for angular-dependent measurements of magnetic thin films and spintronic nanodevices. *IEEE Trans. Magn.* **54**, 1–7 (2018).
29. Avci, C. O. et al. Unidirectional spin Hall magnetoresistance in ferromagnet/normal metal bilayers. *Nat. Phys.* **11**, 570–575 (2015).
30. Vélez, S. et al. Hanle magnetoresistance in thin metal films with strong spin-orbit coupling. *Phys. Rev. Lett.* **116**, 016603 (2016).
31. McKinnon, T., Heinrich, B. & Girt, E. Spacer layer thickness and temperature dependence of interlayer exchange coupling in Co/Ru/Co trilayer structures. *Phys. Rev. B* **104**, 024422 (2021).
32. Ziętek, S. et al. The influence of interlayer exchange coupling in giant magnetoresistive devices on spin diode effect in wide frequency range. *Appl. Phys. Lett.* **107**, 122410 (2015).
33. Ziętek, S. et al. Rectification of radio frequency current in giant magnetoresistance spin valve. *Phys. Rev. B* **91**, 014430 (2015).
34. Tulapurkar, A. A. et al. Spin-torque diode effect in magnetic tunnel junctions. *Nature* **438**, 339–342 (2005).
35. Sankey, J. C. et al. Measurement of the spin-transfer-torque vector in magnetic tunnel junctions. *Nat. Phys.* **4**, 67–71 (2008).
36. Kittel, C. On the theory of ferromagnetic resonance absorption. *Phys. Rev.* **73**, 155–161 (1948).
37. Baselgia, L. et al. Derivation of the resonance frequency from the free energy of ferromagnets. *Phys. Rev. B* **38**, 2237–2242 (1988).
38. Silva, T. J., Lee, C. S., Crawford, T. M. & Rogers, C. T. Inductive measurement of ultrafast magnetization dynamics in thin-film permalloy. *J. Appl. Phys.* **85**, 7849–7862 (1999).
39. Serrano-Guisan, S. et al. Inductive determination of the optimum tunnel barrier thickness in magnetic tunneling junction stacks for spin torque memory applications. *J. Appl. Phys.* **110**, 023906 (2011).
40. Banasik, M. et al. Magnetic properties and magnetization dynamics of magnetic tunnel junction bottom electrode with different buffer layers. *IEEE Trans. Magn.* **51**, 1–4 (2015).
41. Liu, L., Moriyama, T., Ralph, D. C. & Buhrman, R. A. Spin-torque ferromagnetic resonance induced by the spin Hall effect. *Phys. Rev. Lett.* **106**, 036601 (2011).
42. Pai, C.-F. et al. Spin transfer torque devices utilizing the giant spin Hall effect of tungsten. *Appl. Phys. Lett.* **101**, 122404 (2012).
43. Hao, Q. & Xiao, G. Giant spin Hall effect and switching induced by spin-transfer torque in a W/Co40Fe40B20/MgO structure with perpendicular magnetic anisotropy. *Phys. Rev. Appl.* **3**, 034009 (2015).
44. Kim, J. et al. Layer thickness dependence of the current-induced effective field vector in Ta/CoFeB/MgO. *Nat. Mater.* **12**, 240–245 (2013).
45. Nguyen, M.-H. & Pai, C.-F. Spin-orbit torque characterization in a nutshell. *APL Mater.* **9**, 030902 (2021).
46. Ziętek, S. et al. Numerical model of harmonic Hall voltage detection for spintronic devices. *Phys. Rev. B* **106**, 024403 (2022).
47. Avci, C. O. et al. Interplay of spin-orbit torque and thermoelectric effects in ferromagnet/normal-metal bilayers. *Phys. Rev. B* **90**, 224427 (2014).
48. Fritz, K., Wimmer, S., Ebert, H. & Meinert, M. Large spin Hall effect in an amorphous binary alloy. *Phys. Rev. B* **98**, 094433 (2018).
49. Skowroński, W. et al. Angular harmonic Hall voltage and magnetoresistance measurements of Pt/FeCoB and Pt-Ti/FeCoB bilayers for spin Hall conductivity determination. *IEEE Trans. Electron Devices* **68**, 6379–6385 (2021).
50. Grochot, K. et al. Current-induced magnetization switching of exchange-biased NiO heterostructures characterized by spin-orbit torque. *Phys. Rev. Appl.* **15**, 014017 (2021).
51. Lee, K.-S., Lee, S.-W., Min, B.-C. & Lee, K.-J. Threshold current for switching of a perpendicular magnetic layer induced by spin Hall effect. *Appl. Phys. Lett.* **102**, 112410 (2013).
52. Romera, M. et al. Binding events through the mutual synchronization of spintronic nano-neurons. *Nat. Commun.* **13**, 883 (2022).
53. Locatelli, N., Cros, V. & Grollier, J. Spin-torque building blocks. *Nat. Mater.* **13**, 11–20 (2014).
54. Camsari, K. Y., Ganguly, S. & Datta, S. Modular approach to spintronics. *Sci. Rep.* **5**, 10571 (2015).
55. Nomura, H. et al. Reservoir computing with dipole-coupled nanomagnets. *Jpn. J. Appl. Phys.* **58**, 070901 (2019).
56. Akashi, N. et al. A Coupled spintronics neuromorphic approach for high-performance reservoir computing. *Adv. Intell. Syst.* **4**, 2200123 (2022).
57. Gilbert, T. Classics in magnetism: a phenomenological theory of damping in ferromagnetic materials. *IEEE Trans. Magn.* **40**, 3443–3449 (2004).
58. Ralph, D. & Stiles, M. Spin transfer torques. *J. Magn. Magn. Mater.* **320**, 1190–1216 (2008).
59. Ament, S., Rangarajan, N., Parthasarathy, A. & Rakheja, S. Solving the stochastic Landau-Lifshitz-Gilbert-Slonczewski equation for monodomain nanomagnets: a survey and analysis of numerical techniques. Preprint at <http://arxiv.org/abs/1607.04596> (2017).
60. Voss, R. F. "1/f noise" in music: music from 1/f noise. *J. Acoust. Soc. Am.* **63**, 258 (1978).
61. Parkin, S. S. P. Systematic variation of the strength and oscillation period of indirect magnetic exchange coupling through the 3d, 4d, and 5d transition metals. *Phys. Rev. Lett.* **67**, 3598–3601 (1991).
62. Schabes, M. & Aharoni, A. Magnetostatic interaction fields for a three-dimensional array of ferromagnetic cubes. *IEEE Trans. Magn.* **23**, 3882–3888 (1987).
63. Newell, A. J., Williams, W. & Dunlop, D. J. A generalization of the demagnetizing tensor for nonuniform magnetization. *J. Geophys. Res.* **98**, 9551 (1993).
64. Fukushima, H., Nakatani, Y. & Hayashi, N. Volume average demagnetizing tensor of rectangular prisms. *IEEE Trans. Magn.* **34**, 193–198 (1998).
65. Bertotti, G., Mayergoyz, I. D. & Serpico, C. in *Chapter 10—Stochastic Magnetization Dynamics* (eds Bertotti, G., Mayergoyz, I. D. & Serpico, C.) *Nonlinear Magnetization Dynamics in Nanosystems* Elsevier Series in Electromagnetism 271–357 (Elsevier, Oxford, 2009).
66. Brown, W. F. Thermal fluctuations of a single-domain particle. *Phys. Rev.* **130**, 1677–1686 (1963).
67. Kubo, R. & Hashitsume, N. Brownian motion of spins. *Prog. Theor. Exp. Phys.* **46**, 210–220 (1970).

ACKNOWLEDGEMENTS

We thank P. Ogorodnik for a fruitful and insightful discussion. The research project is partially supported by the National Science Centre, Poland project no.2021/40/Q/ST5/00209 (Sheng), the Excellence initiative-research university programme of the AGH University of Science and Technology and by the Polish Ministry of Education and Science under subvention funds for the Institute of Electronics AGH. T.S. and K.G. were supported by the National Science Centre, Poland, Grant No. UMO-2016/23/B/ST3/01430 (SPINORBITRONICS). For the purpose of Open Access, the author has applied a CC-BY public copyright licence to any Author Accepted Manuscript (AAM) version arising from this submission.

AUTHOR CONTRIBUTIONS

J.M. developed the simulation software. S.Z. and J.M. contributed to the model, analysed results and wrote the article. K.G., W.S. and T.S. provided experimental data and extensive feedback on the article.

COMPETING INTERESTS

The authors declare no competing interests.

ADDITIONAL INFORMATION

Supplementary information The online version contains supplementary material available at <https://doi.org/10.1038/s41524-023-01002-x>.

Correspondence and requests for materials should be addressed to Jakub Mojsiejuk or Sławomir Ziętek.

Reprints and permission information is available at <http://www.nature.com/reprints>

Publisher's note Springer Nature remains neutral with regard to jurisdictional claims in published maps and institutional affiliations.



Open Access This article is licensed under a Creative Commons Attribution 4.0 International License, which permits use, sharing, adaptation, distribution and reproduction in any medium or format, as long as you give appropriate credit to the original author(s) and the source, provide a link to the Creative Commons license, and indicate if changes were made. The images or other third party material in this article are included in the article's Creative Commons license, unless indicated otherwise in a credit line to the material. If material is not included in the article's Creative Commons license and your intended use is not permitted by statutory regulation or exceeds the permitted use, you will need to obtain permission directly from the copyright holder. To view a copy of this license, visit <http://creativecommons.org/licenses/by/4.0/>.

© The Author(s) 2023